Additive Manufacturing Frontiers 5 (2026) 200274

Contents lists available at ScienceDirect

Additive Manufacturing Frontiers

journal homepage: www.elsevier.com/locate/amf

Adaptive powder-spreading strategy driven by powder characteristics for high-quality LPBF forming

Yiqi Peng [a], Yaru Fan [a], Yufan Zhao [a,b,*], Hao Wang [c], Sirui Zhang [a], Kenta Aoyagi [d], Seunkyun Yim [d], Akihiko Chiba [d], Xin Lin [a,b,*]

[a] State Key Laboratory of Solidification Processing, Northwestern Polytechnical University, Xi'an, 710072, China
[b] Research & Development Institute of Northwestern Polytechnical University in Shenzhen, Shenzhen, 518063, China
[c] Co-Creation Institute for Advanced Materials, Shimane University, Matsue, 690-8504, Japan
[d] New Industry Creation Hatchery Center (NICHe), Tohoku University, Sendai, 980-8577, Japan

ARTICLE INFO

Keywords:
Powder characteristics
Powder-spreading strategy
Discrete element method
Machine learning

ABSTRACT

Fluctuations in powder characteristics, including particle morphology and size distribution, have a profound impact on the powder bed uniformity and overall fusion quality in laser powder bed fusion (LPBF) processes, ultimately hindering process stability and performance. To address these challenges, this study developed an adaptive powder-spreading strategy that integrates discrete element method (DEM) simulations with in-situ monitoring and machine learning (ML) techniques. A non-spherical particle DEM model was employed to capture the complex dynamic interactions governing powder behavior. The results reveal the competition between the powder-driven inertial and contact effects that dominate the spreading behavior of both gas-atomized (GA) and plasma rotating electrode process (PREP) TC4 powders under varying layer thicknesses and spreading speeds. Building upon this physics-informed understanding, a high-accuracy (93 %) support vector machine model was trained on DEM-generated data and further augmented with experimental measurements to enable rapid and robust optimization of spreading parameters tailored to specific powder characteristics. Under these ML-optimized conditions, the forming quality of PREP and GA-TC4 powders, as quantified by surface roughness (*Ra*), was significantly improved by 26.5 %–37.9 % relative to the equipment default settings. This integrated DEM–ML framework provides a physics-based, efficient, and adaptive pathway for process optimization, significantly reducing the reliance on costly trial-and-error experiments and enhancing the stability, reproducibility, and reliability of LPBF for complex powder systems.

1. Introduction

Powder bed fusion (PBF) additive manufacturing is a critical method for the integrated and lightweight fabrication of complex components in advanced engineering applications [1]. During PBF, powder characteristics such as particle size distribution and particle morphology directly influence the stability of the forming process and the final product quality [2,3]. However, current research remains insufficient to fully elucidate the effects of powder characteristics on the spreading and subsequent fusion processes of powders. Even when powders with identical alloy compositions are used, variations in the powder preparation methods or production batches can cause significant differences in component performance and forming quality, despite the use of similar equipment and process parameters [4–6]. The high sensitivity of the process to powder characteristics limits the stability and scalability of additive manufacturing applications.

As a core factor controlling the forming quality of laser PBF (LPBF), the stability of powder spreading depends on the uniformity and continuity of the powder flow behavior. The ideal flow behavior and spatial packing density of particles are primarily influenced by the particle size distribution [7]. They are further affected synergistically by multiple factors such as particle morphology, surface conditions, and internal porosity [8,9]. For example, the mixing ratio of coarse and fine powders alters the friction and cohesive forces between particles. Irregular particle morphologies promote a "mechanical interlocking" effect that impedes powder flow, whereas surface oxides reduce interparticle adhesion; both factors directly impair powder bed uniformity and thereby ultimately degrade the powder-layer quality [10,11]. The powder morphology also significantly affects the spreading performance, including flowability, packing behavior, and layer uniformity. Schiochet Nasato et al. [12] found that, in contrast to conventional perception, spherical particles do not always perform the best. Spherical particles excel

* Corresponding authors.
E-mail addresses: zhyf90215@nwpu.edu.cn (Y. Zhao), xlin@nwpu.edu.cn (X. Lin).

https://doi.org/10.1016/j.amf.2025.200274
Received 9 October 2025; Received in revised form 10 November 2025; Accepted 21 November 2025
Available online 13 December 2025

at high spreading speeds, whereas flat or low-aspect-ratio non-spherical particles perform better at low speeds. This complex multiscale interaction makes directly observing particle behavior during the dynamic powder-spreading process difficult, leaving the intrinsic correlation and influence mechanisms between the powder characteristics and spreading stability largely unexplored [13].

Slight variations in the powder-spreading parameters can significantly affect the packing density and uniformity of the powder bed. For example, inertial forces dominate the powder motion when the recoater speed is too high, resulting in chain-like accumulation [14,15]. Conversely, the cohesive forces may cause the local powder to collapse when the speed is too low. Both scenarios reduce the packing density and can induce defects in the final product. Meier et al. [16] demonstrated that particle size and adhesion significantly affect the uniformity of the powder layer . Adhesive forces dominate the powder behavior under fine-particle conditions, thereby reducing the layer quality. However, the effects of non-spherical particles and complex dynamic interactions have not been fully considered. Lampitella et al. [17] used simulations to reveal powder distribution, packing density, and particle size evolution under different flow regimes. Le et al. [18] proposed a scanning-based evaluation method and validated its effectiveness using layer thickness uniformity, fusion surface roughness, and powder packing density as indicators. This approach provides a quantitative tool for process optimization. Chen et al. [3,19,20] combined experiments and simulations to systematically investigate the effect of spreading speed on powder-layer quality and packing density. They identified three key mechanisms in the powder-spreading process: cohesion, wall, and penetration effects. These studies indicate that a comprehensive understanding of powder spreading requires not only the identification of key influencing factors but also the development of methods that can capture the complex coupling between powder characteristics and process parameters. Such an approach is essential for elucidating the fundamental mechanisms of powder spreading and the systematic optimization of additive manufacturing processes.

Although previous studies have experimentally optimized powder-spreading parameters, two major bottlenecks remain [21]. First, the relationship between the spreading parameters and fusion quality is highly complex. Traditional trial-and-error methods typically require hundreds of experimental runs, which results in high costs. This makes the rapid and accurate optimization of process parameters across different powders and applications challenging. Second, most existing theoretical models assume ideal spherical particles and neglect morphological heterogeneity and dynamic particle interactions. This limits the ability to effectively reveal the coupling mechanisms between powder characteristics and process parameters, highlighting the need for approaches that can efficiently capture dynamic particle interactions and optimize the process parameters.

To address these challenges, this paper proposes an adaptive powder-spreading strategy driven by powder characteristics, which integrates discrete element method (DEM) simulations calibrated using in-situ monitoring with a machine learning (ML) model to rapidly generate large-scale datasets and efficiently optimize the spreading parameters of gas-atomized (GA) and plasma-rotating electrode process (PREP) powders. This approach focuses on improving the fusion quality (Ra of formed samples), which is closely related to the powder-spreading quality (powder-bed packing density). Compared with the overall density, the fusion quality serves as a more direct and sensitive indicator, being less affected by other factors, thus enabling higher prediction accuracy, while remaining crucial for ensuring forming quality and mechanical performance. By combining DEM modeling with in-situ experimental monitoring, this study revealed the dynamic coupling mechanism between the inertial and contact effects in non-ideal powder particles. A support vector machine (SVM) ML model was developed based on datasets generated from DEM simulations, enabling the rapid optimization of spreading parameters (layer thickness and spreading speed) for complex powder systems. The proposed approach significantly reduces the surface roughness of the fused powder bed, lowers trial-and-error costs, and advances additive manufacturing by promoting the synergistic integration of ML and physics-based process optimization.

Table 1
Chemical composition of the three TC4 powders (wt%).

	C	Al	V	Fe	O	N	H
PREP25–75	0.005	5.72	3.95	0.20	0.076	0.002	0.0036
PREP0–53	0.006	6.05	4.08	0.18	0.088	0.005	0.0055
GA0–53	0.008	5.84	3.90	0.031	0.108	0.011	0.0020

2. Experiments

2.1. Materials

The experimental materials included three types of TC4 powders produced by SINO-EURO Materials Technologies of Xi'an Co., Ltd. Their chemical compositions are listed in Table 1. The three types of powders (GA0–53, PREP0–53, and PREP25–75) were named based on their preparation methods and differences in particle size. GA0–53 was prepared using the GA method, whereas PREP0–53 and PREP25–75 were prepared using the PREP approach. The morphologies of the three powders were characterized using scanning electron microscopy (SEM) with statistical image analysis, and their particle size distributions were obtained by measuring and statistically analyzing at least 5000 particles from the SEM images. Their morphological features and particle size distributions are shown in Fig. 1. The flowability of the powders was measured using a Hall flowmeter. Compared with the PREP powders, the GA powders exhibited poorer flowability and were unable to flow freely through the Hall flowmeter. The powders produced using the PREP method exhibited higher sphericity, whereas those produced using the GA method contained a greater number of satellite particles. The apparent and tap densities of the powders were also measured. The data related to the powder characteristics are summarized in Table 2.

Because of the significant differences in powder characteristics, traditional approaches often require many experiments to determine the optimal process parameters for different types or batches of powders. In this study, a uniform experimental design was applied to the GA0–53, PREP0–53, and PREP25–75 powders. The BLT-S210 system was employed in combination with the manufacturer-recommended default powder-spreading parameters for TC4 (parameter set 6) to select six representative sets of process parameters (see Table 3) for 10 mm × 10 mm × 10 mm bulk forming experiments, thereby effectively reducing the experimental time and cost.

2.2. In-situ monitoring and DEM simulation

In this study, a DEM model incorporating non-spherical particles was developed in conjunction with an in-situ monitoring system (Fig. 2) to address the limited dynamic characterization capability of commercial PBF equipment. Actual powder morphologies were reconstructed using three-dimensional laser scanning (shape factor = 0.3–0.7), and three representative types of non-ideal particles were embedded into the DEM model based on their real shapes and proportions: large particles with adhered fines (4 %), bispherical particles (15 %), and irregular ellipsoidal particles (8 %), whereas the remaining 73 % were ideal spherical particles. The classification and proportion of these particle types were determined based on statistical analysis of the SEM images (Fig. 1). Compared with the conventional idealized spherical particle assumption, the inclusion of non-spherical particles improved the stability of the interparticle contact force chains by approximately 30 %–45 %.

In the DEM simulation, a non-linear elastic Hertz–Mindlin no-slip contact model [22] was employed, and energy dissipation was implemented through viscous damping to simulate the dynamic behavior of

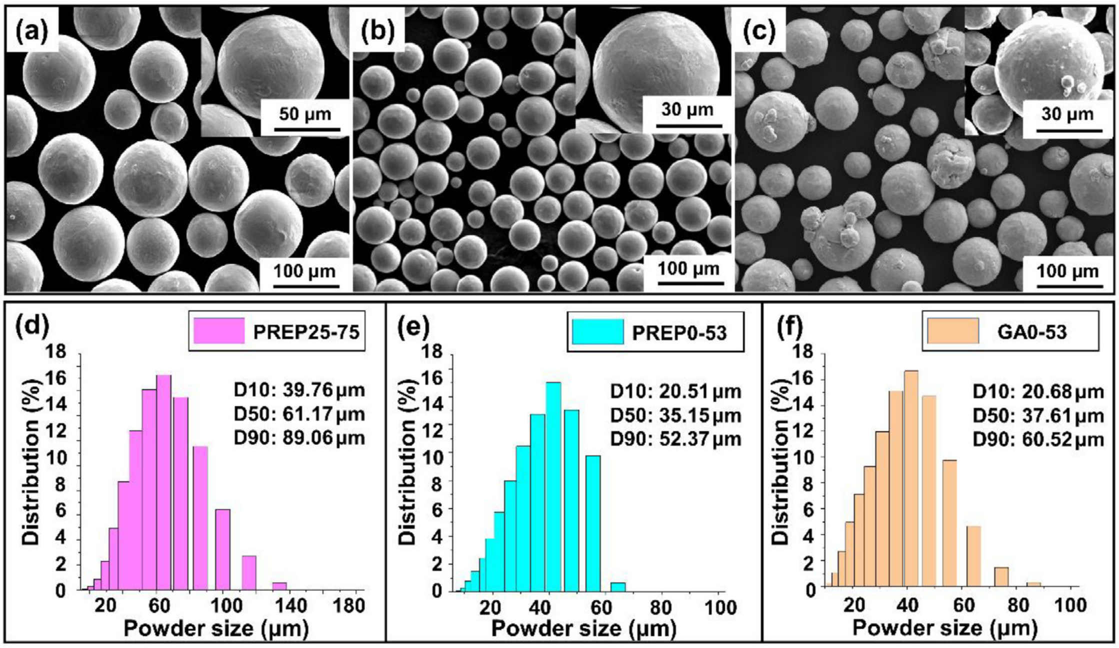

Fig. 1. SEM images of TC4 alloy powders: (a) PREP25–75, (b) PREP0–53, and (c) GA0–53; The particle size distributions of TC4 powders: (d) PREP25–75, (e) PREP0–53, and (f) GA0–53; The naming of the three types of powders was based on their preparation method and differences in particle size.

Table 2
Particle size distribution, flowability, and density of the three powders.

	D_{10} (μm)	D_{50} (μm)	D_{90} (μm)	Flowability index (g/50 s)	Apparent density (g/cm^3)	Tap density (g/cm^3)
PREP25–75	39.76	61.17	89.06	24.58	2.60	2.35
PREP0–53	20.51	35.15	52.37	23.08	2.47	2.29
GA0–53	20.68	37.61	60.52	–	2.33	2.17

Table 3
LPBF processing parameters.

No.	Laser power (W)	Scanning speed (mm/s)	Spot diameter (mm)	Layer thickness (μm)	Spreading speed (mm/s)	Laser energy density (J/mm)
1	155	1200	0.1	20	95	53.8
2				30	155	35.9
3				40	275	26.9
4				60	155	17.9
5				80	35	13.5
6				100	215	10.4

the powder [23]; the derivation of the contact law and energy dissipation method are detailed in reference [24]. The powders used were TC4 alloys, including PREP25–75, PREP0–53, and GA0–53. The interparticle friction, rolling resistance, and restitution coefficients were selected based on experimental data from Ref. [25], whereas the tap density and particle size distribution were determined from experimental measurements (listed in Table 2). Because the average particle size exceeded 20 μm, van der Waals and capillary forces could be neglected, and the powder behavior was primarily dominated by friction and collisions. Therefore, the Hertz–Mindlin model adequately represented the main interparticle interactions, providing a close approximation of the dynamic behavior of actual metal powders.

A high-speed imaging (Revealer-5KF10M) platform (sampling rate ≥ 1000 fps) was used for in-situ monitoring, enabling high-precision tracking of particle migration trajectories (≥ 5×10^3 particles per frame) and sensitive detection of local changes in the repose angle of the powder bed (detection sensitivity 0.3°–0.8°) during the spreading process. By comparing the in-situ measured powder bed angles with those predicted by the DEM simulation (as shown in Section 4.2), the DEM model (developed using DEMSlab software) was validated, providing crucial insights into powder flow mechanisms and guidance for optimizing LPBF spreading parameters [26]. Additionally, the packing density can be quantitatively evaluated by binarizing the vertical views of the generated powder bed from both the experiments and simulations (Figs. 2(a_3) and (b_2)), providing a basis for analyzing packing density.

2.3. SVM model

To address the problem of the insufficient generalization ability of traditional ML models under small-sample conditions, a novel simulation-driven ML collaborative optimization framework is proposed. This framework aims to reduce the experimental workload significantly while efficiently obtaining sample data points, thereby improving the prediction accuracy and generalization performance of the ML model.

Based on high-precision DEM simulations calibrated using in-situ monitoring, a dataset of 63 samples (simulation: experimental = 5:2) was generated to balance diversity and physical fidelity, covering key physical indicators such as the packing density and porosity of the powder bed. Using this dataset, an SVM model was trained to achieve a rapid and accurate optimization of the spreading parameters (layer thickness and spreading speed). Using the ±1 classification scheme of the SVM,

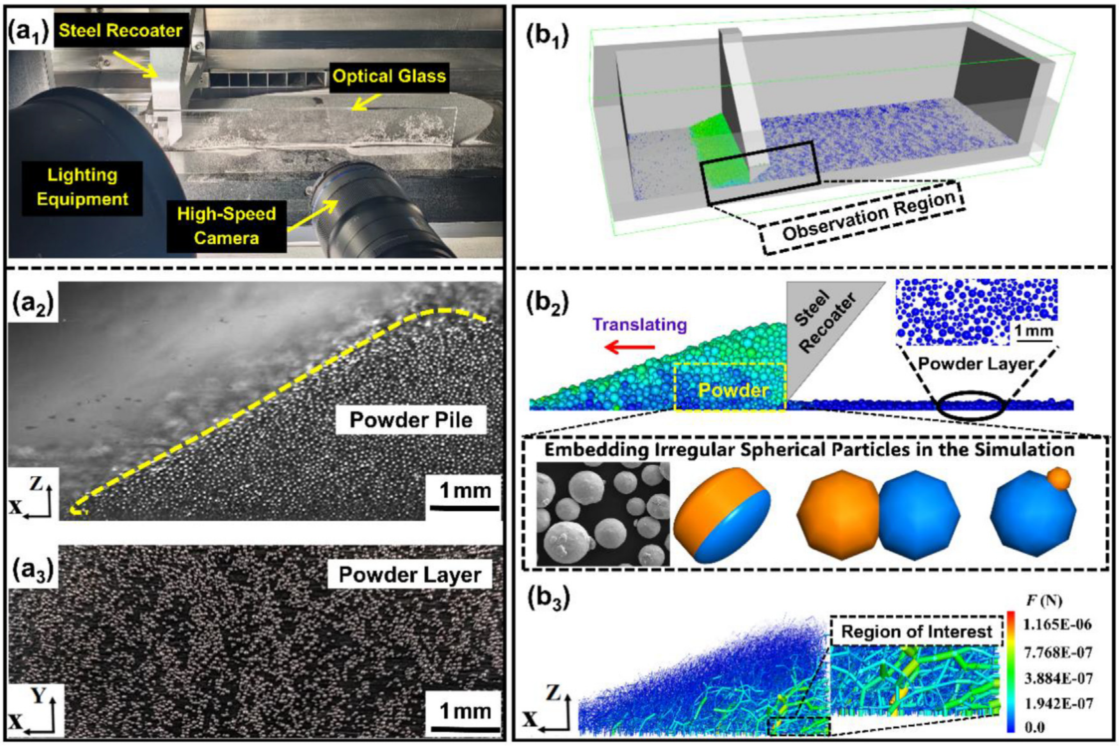

Fig. 2. In-situ monitoring and DEM simulation diagram of powder motion: (a_1) In-situ characterization platform built-in LPBF warehouse; (a_2) Powder pile during the experiment; (a_3) Vertical view of generated powder bed; (b_1) DEM simulation under the consistent working conditions; (b_2) Powder layer and pile during the DEM simulation; (b_3) Force chain diagram captured from the DEM simulation.

samples above the mean packing density and below the mean Ra were labeled as "1" and others as "–1." The mean was used as the threshold because a uniformly designed experiment ensured a balanced dataset without outliers. The dataset was randomly divided into training and testing subsets at a ratio of 8:2 to ensure sufficient data for both model learning and performance evaluation.

The dataset was used to train an SVM model with an RBF kernel. Five-fold cross-validation was employed to evaluate the performance of the model and enhance its generalization ability under small-sample conditions while simultaneously optimizing the hyperparameters ($C = 100$, gamma = 0.01). This approach enables rapid and precise optimization of the spreading parameters (layer thickness and spreading speed) and ensures stable model performance.

3. Results

Owing to the multiple reflection effects during the interaction between the laser and powder bed, the packing density of the powder bed directly affects the energy absorption rate, melt pool stability, and fusion quality in the LPBF process [27]. The roughness (*Ra*) of the fused upper surface, as a quantitative evaluation index of fusion quality, reflects the final synergy between powder spreading and laser melting during the LPBF process [28,29]. To investigate the stacking and forming characteristics of powder systems with varying properties during the dynamic powder-spreading process, this study systematically analyzed the powder-bed packing density and evolution of the fused upper surface quality for three types of powders with different powder-spreading parameter combinations (listed in Table 3).

3.1. Packing density and fusion quality of three powders

Fig. 3(a) shows the changes in the powder-bed packing density for the three powders under six sets of powder-spreading parameters, and the corresponding powder-bed morphologies under different parameter

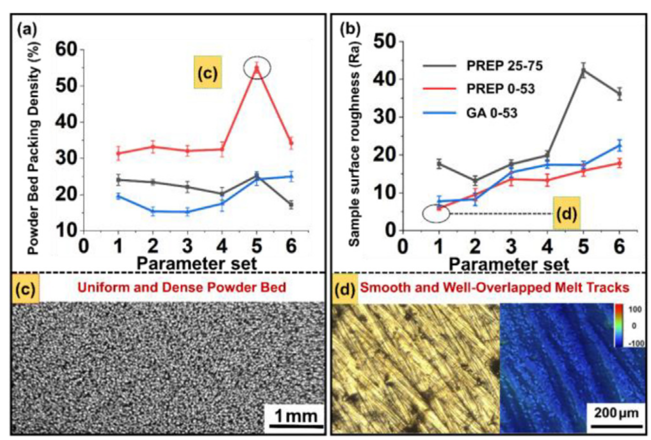

Fig. 3. Changes in (a) powder-bed packing density and (b) surface roughness for three powders under six sets of powder-spreading parameters (Table 3); Specified images of (c) powder layer and (d) fused surface morphology corresponding to the cases marked in (a) and (b), respectively.

sets are shown in Supplementary materials Fig. S1. The PREP0–53 powder achieved the highest packing density of approximately 60 % and uniform powder arrangement under parameter set 5 (Fig. 3(c)). In contrast, the PREP25–75 powder had a markedly lower density (approximately 20 %–28 %), probably because of the presence of larger particles that reduced the flowability and filling efficiency [30]. The GA0–53 powder demonstrated the lowest overall packing density (15 %–25 %), likely because its poor particle sphericity and flowability hindered uniform spreading and left unfilled voids between the powders [31].

Figs. 3(b) and 4 illustrate the variation in the surface roughness (*Ra*) of the specimens fabricated with the three types of powder under six sets of spreading parameters. The highest powder-bed packing density

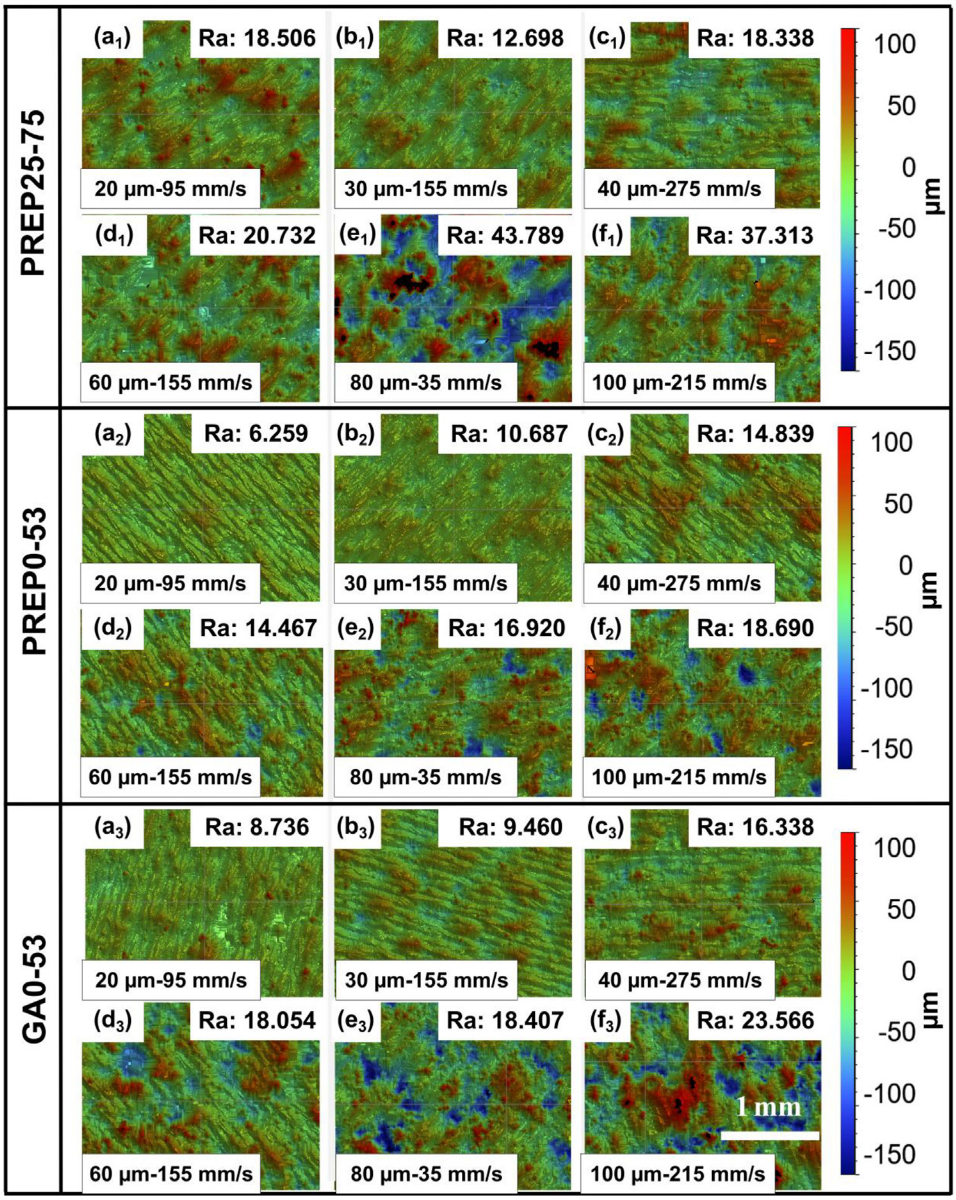

Fig. 4. Surface morphologies of the fused layers under six sets of powder-spreading parameters (Table 3) for three powders: (a_1–f_1) PREP25–75; (a_2–f_2) PREP0–53; (a_3–f_3) GA0–53.

did not correspond to the lowest surface roughness. PREP0–53 powder achieved its maximum packing density under parameter set 5 (35 mm/s spreading speed and 80 μm layer thickness). However, the minimum *Ra* value (6.256 μm) of this powder occurred under parameter set 1 (as shown in Fig. 4(a_2), where the fusion surface was continuous with a good overlap). This discrepancy can be attributed to the interplay between packing density, laser energy absorption, and melt pool stability. At high layer thicknesses, an excessive packing density can reduce laser penetration and remelting efficiency, leading to melt pool instability and increased surface roughness [32,33].

Compared with the PREP0–53 powder, the fusion quality of the PREP25–75 powder under parameter set 5 was significantly poorer (*Ra* > 40 μm, Figs. 4(e_1) & (f_1)). It is speculated that large powder particles are more prone to form an unstable melt pool under the same spreading conditions, consequently increasing the surface roughness.

The fusion *Ra* of the GA0–53 powder consistently remained within the range of 15–30 μm. Its minimum value (8.736 μm), coinciding with that of the PREP0–53 powder, also appeared under parameter set 1 (Fig. 4(a_3)). However, the packing density achieved with parameter set 1 was only 15 %–25 %, significantly lower than that of PREP0–53 under the same set. This demonstrates that a relatively low powder-bed packing density can also yield a favorable fusion surface quality, which further confirms that the optimal fusion quality does not solely depend on the maximum packing density but rather on achieving a balance between sufficient powder presence for laser absorption and maintaining melt pool stability.

In other words, an excellent fusion quality fundamentally results from the synergistic interaction between a specific laser energy input and a powder bed with an appropriate packing density. Achieving a high fusion quality with a low-packing-density powder bed tends to be stochastic, and the corresponding laser energy process window is narrow. Therefore, based on a comprehensive evaluation of the powder-bed packing density and fusion quality, this study assigned labels for the SVM quality classification (as detailed in Section 3.2) to identify optimized spreading parameters with broader applicability.

Table 4
SVM used classification results obtained from experimental data.

Powder	Layer thickness (μm)	Spreading speed(mm/s)	Energy density of laser (J/mm)	Packing density (%)	*Ra* (μm)	Classification
PREP	20	95	53.8	24.064	18.506	1
25–75	30	155	35.9	23.426	12.338	1
	40	275	26.9	22.092	18.338	−1
	60	155	17.9	20.233	20.732	−1
	80	35	13.5	25.181	43.789	−1
	100	215	10.4	17.215	37.313	−1
PREP	20	95	53.8	31.338	6.259	1
0–53	30	155	35.9	33.181	10.687	1
	40	275	26.9	32.036	14.839	1
	60	155	17.9	32.463	14.467	1
	80	35	13.5	55.057	16.92	1
	100	215	10.4	34.193	18.69	−1
GA	20	95	53.8	19.560	8.736	1
0–53	30	155	35.9	15.361	9.46	−1
	40	275	26.9	15.211	16.338	−1
	60	155	17.9	17.494	18.054	−1
	80	35	13.5	24.199	18.047	−1
	100	215	10.4	24.994	23.566	−1

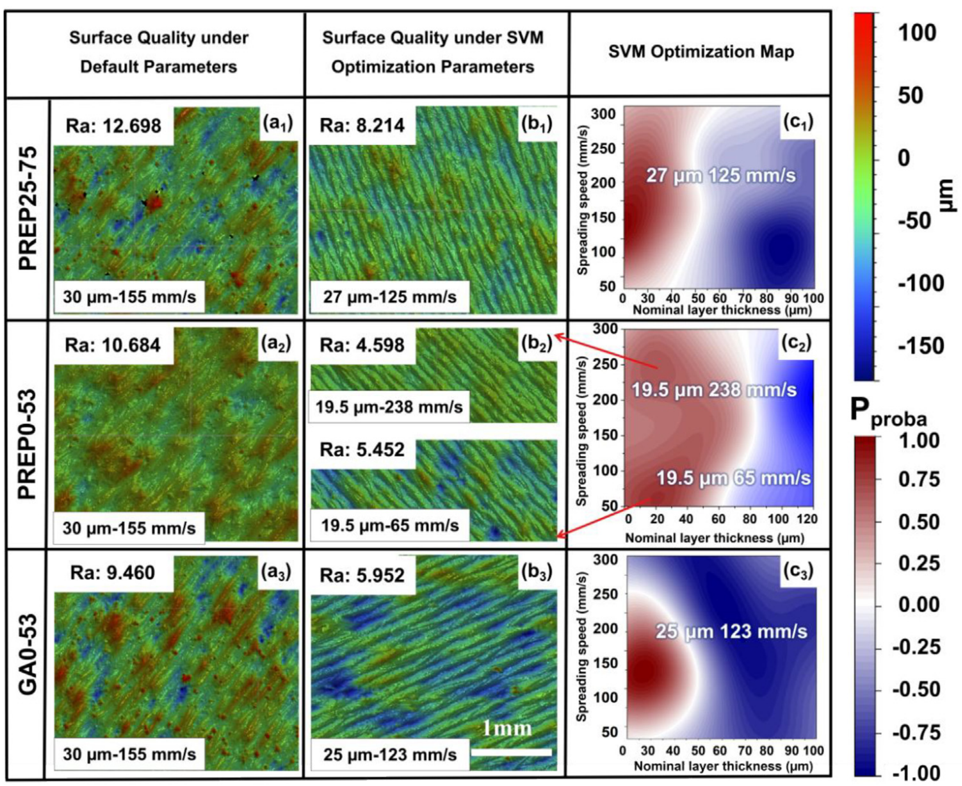

Fig. 5. SVM optimization maps and comparison of forming quality under default settings of the LPBF equipment and SVM-optimized parameters for three powders: (a_1–c_1) PREP25–75; (a_2–c_2) PREP0–53; (a_3–c_3) GA0–53.

3.2. Optimization of powder-spreading parameters based on SVM

The classification results for the experimental dataset are listed in Table 4, and the results for the DEM-augmented dataset are provided in **Supplementary materials Table S1.**

Based on the aforementioned classification criteria (Section 2.3), the SVM model was trained and validated using a dataset comprising 45 simulation datasets generated using the DEM and 18 experimental datasets. The final model achieved a prediction accuracy of 93 %, demonstrating a good predictive precision. Subsequently, the SVM optimization map shown in Fig. 5(c) was obtained. The predicted probability values (P_{proba}) were used to represent the confidence level of each parameter combination, with values closer to 1 indicating a higher confidence in achieving superior fusion quality and powder packing density. Accordingly, the color gradient from red to blue reflects the transition from superior to inferior performance, where the red regions correspond to the optimal process window for achieving high-quality surface fusion and high packing density.

Fig. 6 compares the fusion quality under the default powder-spreading parameters (control group) of the LPBF equipment (Fig. 6(a)) and the optimized ML parameters (Fig. 6(b)). The results showed that the optimized parameters yielded smoother and flatter melt tracks with lower surface roughness. Among these, the PREP0–53 powder fused surface Ra value improved significantly, decreasing from 10.687 μm in the control group (using manufacturer-recommended default powder-spreading parameters, Fig. 4(b_2)) to 4.598 μm (using optimized powder-

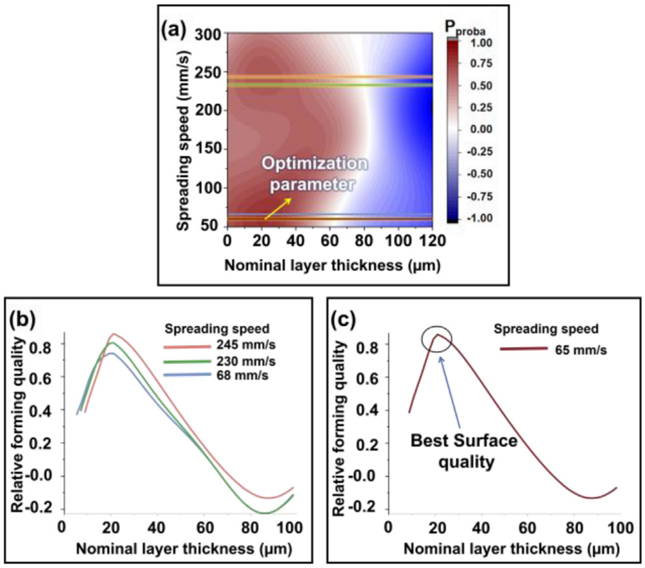

Fig. 6. Effect of layer thickness on forming quality under different spreading speeds for PREP0–53 powder based on (a) SVM optimization map with the profiles of (b) three spreading speeds (265, 230, 68 mm/s) and (c) the optimized spreading speed (65 mm/s).

spreading parameters, Fig. 6(b_2)). The melt track morphology became more continuous and the surface flatness was notably enhanced. Additionally, PREP0–53, characterized by a small powder particle size, high sphericity, and good flowability, achieved superior fusion quality compared with the control group under both low and high powder-spreading speeds. In contrast, PREP25–75 and GA0–53, owing to their larger powder particle sizes or irregular morphologies, respectively, achieved a balance between flowability and pileability only at medium powder-spreading speeds, resulting in a single optimal parameter. A detailed analysis of this mechanism is provided in Section 4.2.

The optimal powder-spreading thicknesses for the three types of powders were concentrated in a relatively narrow range (19.5–27 μm). This was primarily because of the laser energy conditions applied in this study (laser power of 155 W and scanning speed of 1200 mm/s); an excessive thickness can prevent complete laser penetration, leading to a lack of fusion. Further analysis of the optimization map of the PREP0–53 powder (Fig. 6) revealed that at a fixed spreading speed, the fusion quality initially improves and then deteriorates as the thickness increases. Initially, an increase in thickness enhances the spreading uniformity and fusion quality. However, when the thickness exceeds a critical value, the laser energy becomes insufficient for full penetration, resulting in inadequate remelting. Additionally, as the spreading speed increases, the optimal thickness correspondingly increases (Figs. 6(b) and (c)). This is because an increased spreading speed reduces the powder quantity per unit area (lower powder layer density), necessitating a thicker layer to compensate for the total powder amount and maintain a match between the laser energy and powder-melting requirements.

4. Discussion

This study conducted fusion experiments using the LPBF equipment with the default laser parameters for TC4 (laser power: 155 W, scanning speed: 1200 mm/s). The default powder-spreading parameters (nominal layer thickness: 30 μm, spreading speed: 155 mm/s) were used as the control group. Through rapid parameter optimization of the SVM model, it was found that under the laser energy conditions used in this study, the optimal powder layer thickness was concentrated within the range of 19.5–27 μm. This optimization result indicated that under the given laser energy input conditions, the powder layer thickness required for excellent fusion quality has a certain adaptive range [34]. Notably, within the parameter regime involved in this study, the optimized spreading speed variation range was relatively broad. Compared with the laser energy adaptability in terms of layer thickness, the influence mechanism of the spreading speed on the powder motion state and corresponding spreading quality is more complex. Therefore, the discussion section is based on experimental results combined with numerical simulations to focus on analyzing the dynamic behavior of powders with different features as the spreading speed changes, thereby establishing an association mechanism between powder characteristics and adaptively optimized spreading parameters.

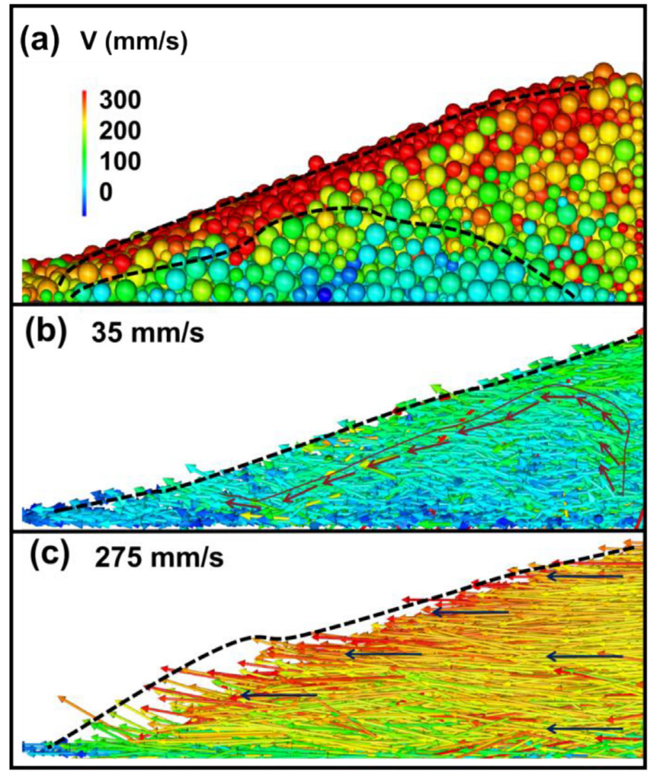

Fig. 7. Simulated diagram of (a) particle motion speed zones during powder spreading at various spreading speeds of (b) 35 mm/s and (c) 275 mm/s.

4.1. Deposition mechanism of spreading powder

Based on in-situ monitoring and DEM simulations, the dynamic behavior of powder particles, including their velocity, direction, and force state within the powder bed, was analyzed at different spreading speeds. The analysis showed that the dynamic behavior in the powder-spreading process is primarily governed by the inertial and contact effects [3,20].

4.1.1. Inertial effect

The inertial effect is primarily manifested by the change in the particle motion state of the powder pile in front of the scraper with variations in spreading speed. As shown in Fig. 7(a), the particle motion speed of the outer layer of the powder pile is relatively high, with particles flowing downward along the slope, whereas the internal particle motion speed of the powder pile and powder near the substrate is lesser. The entire powder pile shifts as the scraper moves [35]. Under low spreading speed conditions, the inertial effect is weak, and the powder pile in front of the scraper exhibits a combined motion mechanism of flow and sliding (Fig. 7(b)). The particle system has sufficient time and probability for reorganization and migration, enabling the effective filling of voids between powder particles and achieving a higher packing density. As the spreading speed increases, particle motion enters the

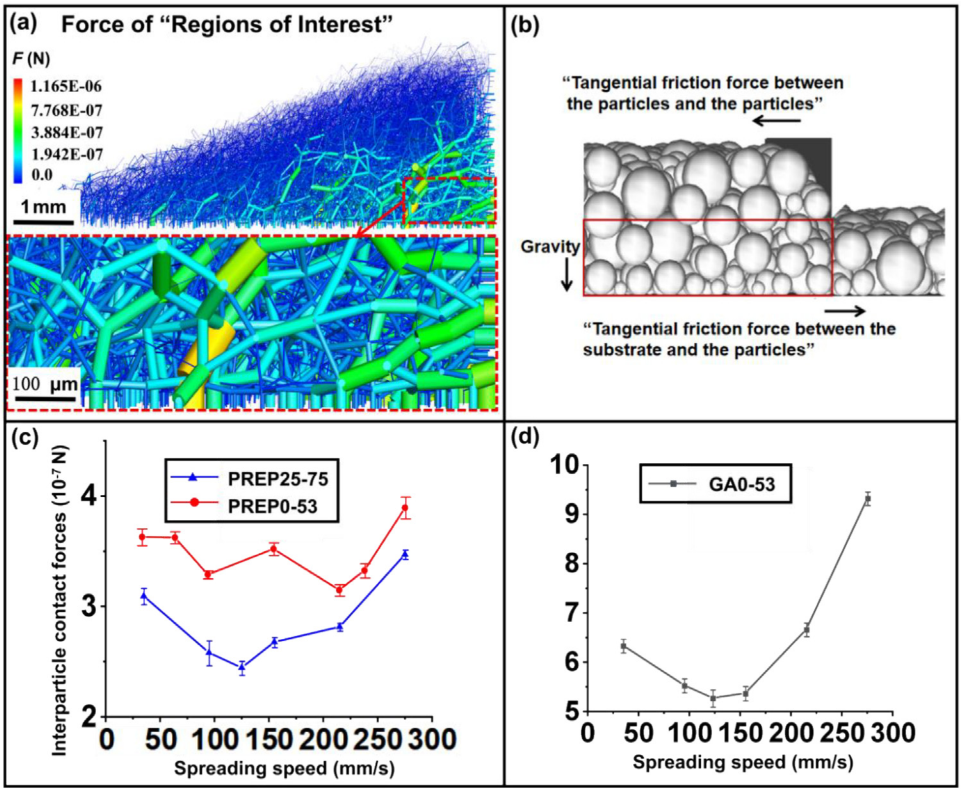

Fig. 8. Forces of regions of interest: (a) Force chain transmission paths for PREP0–53 powder under spreading speed of 100 mm/s; (b) Schematic of contact forces within particles; (c), (d) Simulated results of interparticle contact forces for three powders.

"inertial effect"- dominated status. At this point, the front powder pile tends to be in a rigid solid state. It is primarily driven to move forward along the direction of the scraper advancement, with a significant reduction in the relative flow and sliding between the internal particles (Fig. 7(c)), which is detrimental to deposition spreading. In particular, at the front edge of the powder pile, under the impact of a high-speed moving scraper, some particles detach from the original pile, causing the powder pile to tend toward a loose state, which often results in a decrease in the packing density of the powder bed.

4.1.2. Contact effect

The region of interest shown in Fig. 8(a) corresponds to the area where particles are about to be acted upon by the scraper and subsequently deposited into the powder bed. This is the key region involved in the formation of powder bed structures during powder spreading [36]. To ensure the inclusion of particles simultaneously contacting the scraper and the substrate, thereby capturing all force chain transmission paths for these particles, the dimensions of the region of interest are set to 200 μm in width multiplied by the scraper height. The force states of the particles within this region directly affect the powder bed quality [37]. Particles are primarily subjected to forces including gravity, the frictional force generated along the scraper motion direction from contacts between the upper-layer particles (driven by the scraper) and the particles in the lower region of interest layer, and the transverse frictional force between the bottom particles and the substrate (Fig. 8(b)). During powder spreading, the contact force between the upper-layer particles is a critical factor that influences the powder bed quality. When the contact force is excessive, the resulting friction component opposing the gravitational direction hinders the downward filling behavior of the particles under gravity [38]. This significantly weakens the vertical flowability of the powder, thereby leading to the formation of voids in the local area at the bottom, which reduces the density and uniformity of the powder bed.

Table 5
The particle coordination number (n) under different spreading speeds.

	35 mm/s	95 mm/s	155 mm/s	215 mm/s	275 mm/s
PREP25–75	8	6	6	7	9
PREP0–53	10	7	8	9	9
GA0–53	11	9	8	12	11

Based on Figs. 8(c) and (d), the interparticle contact forces of the three powders initially decreased with an increase in the powder-spreading speed and then subsequently increased. This was owing to the continual variations in the particle arrangement and stress states under different spreading speeds, leading to changes in the particle coordination number (n) and elastic contact force between particles (F). The overall magnitude of the interparticle contact force (N) is determined using $N = nF$. Based on the DEM numerical modeling, n was statistically analyzed under different spreading speeds, and the results are presented in Table 5. The powder particles transitioned from a static close-packed state (with a larger n) to a medium-low speed rolling state (with decreasing n), during which F changed slightly (the magnitude of the forces can be observed in the particle force chain structures shown in Figs. 10, 11, and 12) and N began to decrease. As the spreading speed increased, the particles were propelled during the motion, with n remaining largely unchanged, whereas F increased, leading to an increase in N. Additionally, under the same set of spreading parameters, the contact force between the GA0–53 particles was significantly greater than that of the other two powders. This can be primarily attributed to the higher proportion of irregularly shaped particles in the GA powder, which results in a larger n and, consequently, a greater N.

Based on the above analysis, the dynamic behavior of the powder-spreading process is jointly influenced by the inertial and contact effects. In other words, both significant inertial effect and large contact forces

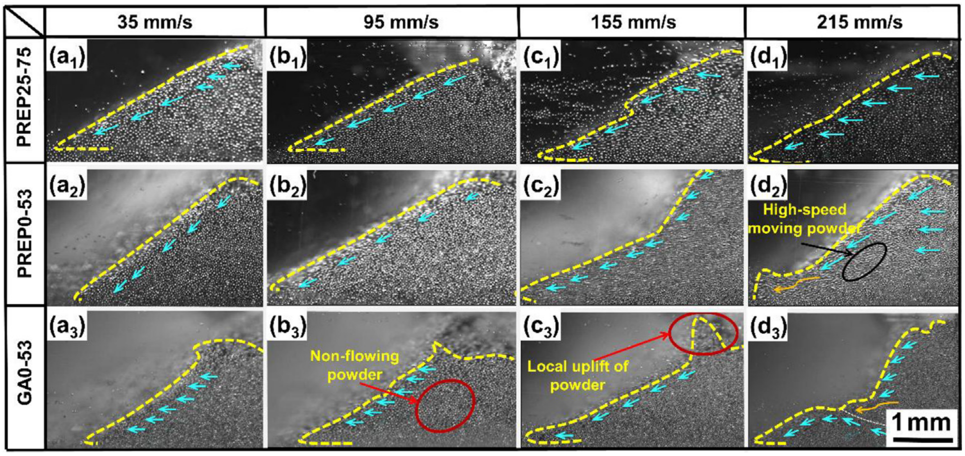

Fig. 9. In-situ monitoring of powder-spreading behaviors at different spreading speeds for (a_1–d_1) PREP25–75, (a_2–d_2) PREP0–53, and (a_3–d_3) GA0–53.

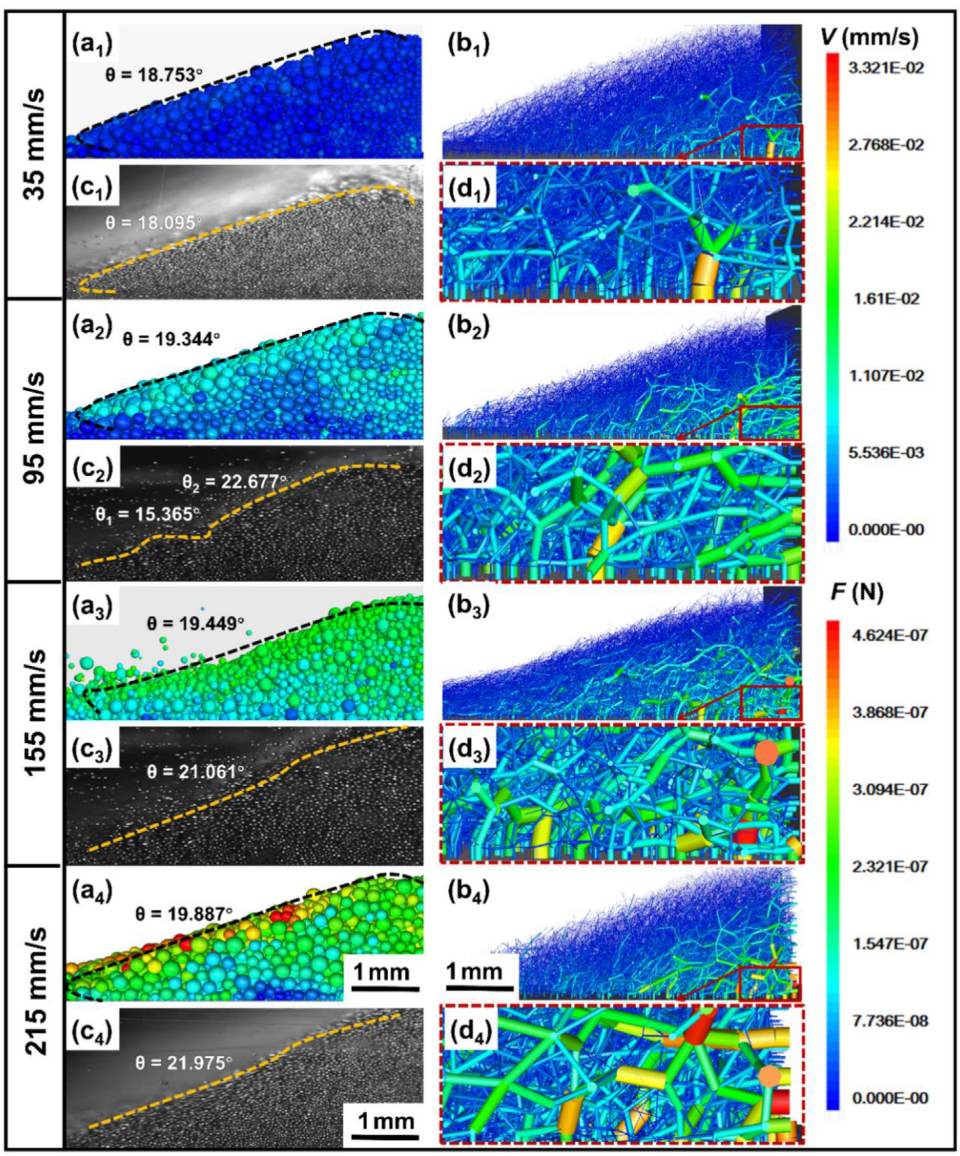

Fig. 10. Powder motion speed and force chain within the powder piles of PREP25–75 under different spreading speeds of (a_1–d_1) 35 mm/s, (a_2–d_2) 95 mm/s, (a_3–d_3) 155 mm/s, and (a_4–d_4) 215 mm/s; θ is the angle of repose of the powder pile.

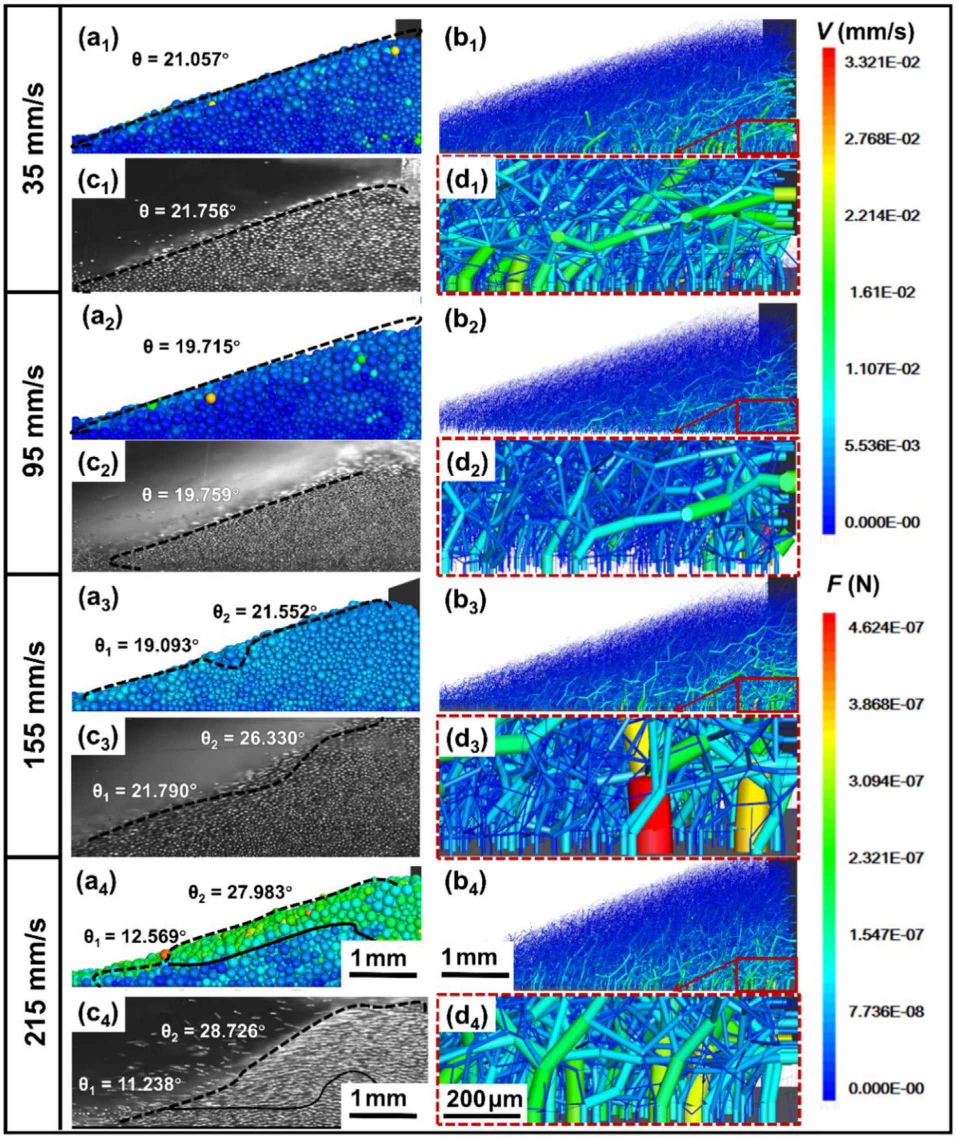

Fig. 11. Powder motion speed and force chain within the powder piles of PREP0–53 under different spreading speeds of (a_1–d_1) 35 mm/s, (a_2–d_2) 95 mm/s, (a_3–d_3) 155 mm/s, and (a_4–d_4) 215 mm/s; θ is the angle of repose of the powder pile.

are detrimental to forming a uniform and dense powder layer. The inertial effect becomes more pronounced as the powder-spreading speed increases, whereas the contact effect is generally present and initially decreases; thereafter, it increases with the increase in powder-spreading speed. Based on the dynamic behavior mechanism of the powder and force analysis, the underlying mechanisms linking the powder characteristics to adaptive, optimized powder-spreading parameters will be further elucidated.

4.2. Dynamic behavior and optimization mechanism in powder spreading

This section, combining in-situ monitoring of the three powders with DEM simulation, will further reveal the dynamic evolution behavior of inertial and contact effects in powder systems with different features. Figs. 9 (a_1–d_1) and 10 show the motion characteristics and stress status of the PREP25–75 powder particles at different spreading speeds. In the medium- to low-speed range (35–155 mm/s), the inertial effect was weak, and the powder particles in the powder pile in front of the scraper flowed downward along the slope while sliding forward with the scraper, with the inclination angle of the powder pile remaining stable at approximately 19° (Figs. 9(a_1) and 10(a_1)–(a_3)). Within this stage, as the spreading speed increased, *N* decreased from 3.6×10^{-7} to 3.4×10^{-7} N continuously owing to the reduction in *n* (Figs. 8(c) and 10(d_2)), and the packing density stabilized at 20 %–25 % (see Section 3.1). In the high-speed stage (≥ 215 mm/s), the inertial effect intensified, resulting in a significant increase in high-speed moving particles in the powder pile ahead of the scraper (red and yellow particles in Fig. 10(a_4) increase in proportion). At this point, the relative flow and sliding between the internal particles decreased notably; simultaneously, *F* increased and *N* increased to (Fig. 10(d_4)). The flow and deposition of the powder pile particles along the gravitational direction were restricted, resulting in the powder-bed packing density dropping below 18 %. This phenomenon indicates that under high-speed powder-spreading conditions, inertia-driven restricted gravitational flow and loose packing are key factors restricting uniform powder spreading.

Figs. 9 (a_2–d_2) and 11 show the motion characteristics and stress status of the PREP0–53 powder particles at different spreading speeds. In the low powder-spreading speed range (35–95 mm/s), the inertial effect was weak, and the particles transitioned from a static close-packed state to a combined motion of flow and sliding. As the spreading speed increased, the PREP0–53 powder exhibited a dynamic evolution trend similar to that of the PREP25–75 powder, where *n* decreased, caus-

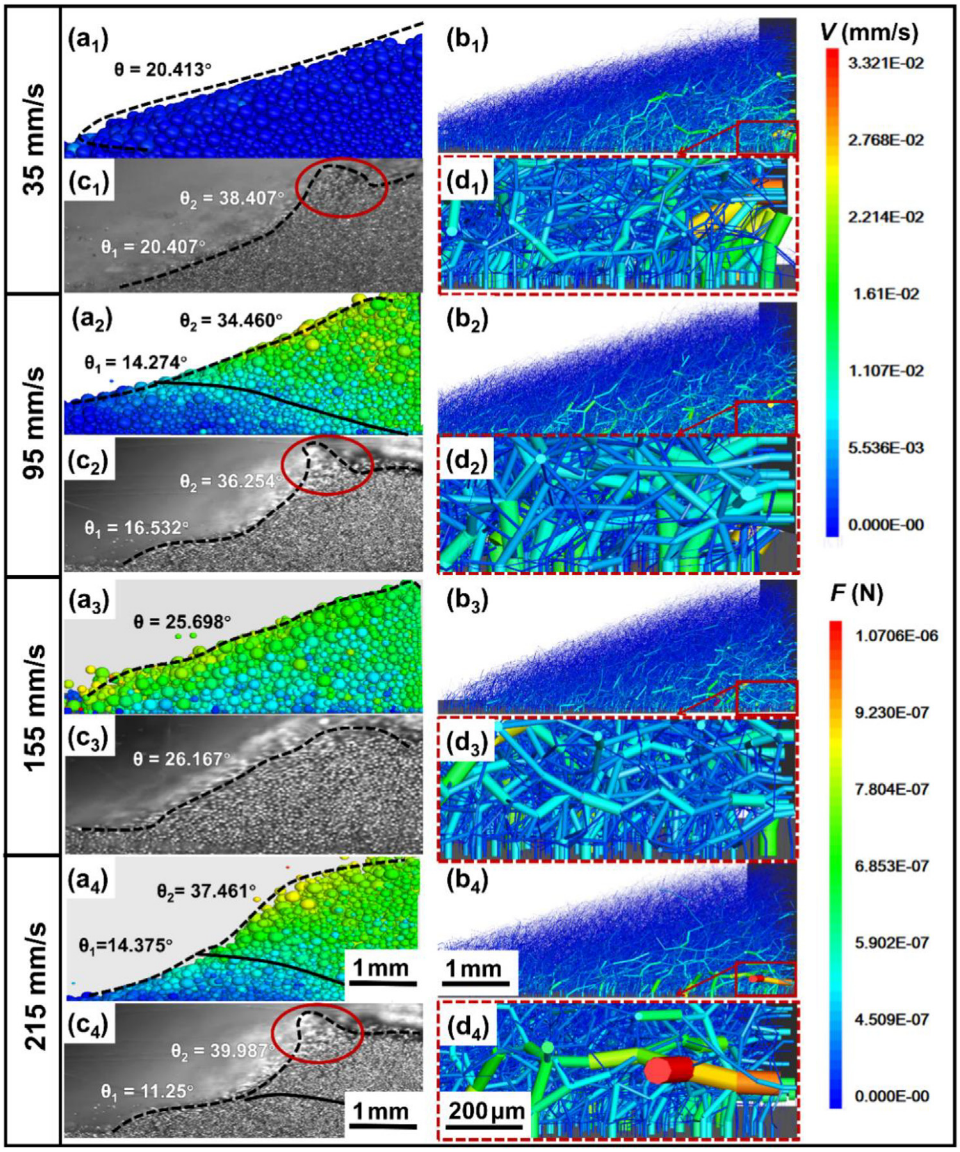

Fig. 12. Powder motion speed and force chain within the powder piles of GA0–53 under different spreading speeds of (a_1–d_1) 35 mm/s, (a_2–d_2) 95 mm/s, (a_3–d_3) 155 mm/s, and (a_4–d_4) 215 mm/s; θ is the angle of repose of the powder pile.

ing N to decrease by approximately 23 %, from about 3.1×10^{-7} to 2.4×10^{-7} N (Figs. 8(c) and 11(d2)). At medium speed (155 mm/s), the particle velocity in the powder pile ahead of the scraper increased, and the entire pile moved uniformly (Fig. 11(a_3)). The powder pile adopted a close-packed state with an increase in n and N (Fig. 11(d_3)). The strong interparticle friction and mechanical interlocking hindered the downward filling behavior of particles under gravity, weakening the vertical flowability and reducing the density and uniformity of the powder bed. At a high speed (215 mm/s), the inertial effect intensified. The powder pile ahead of the scraper exhibited velocity partitioning; the upper layer moved predominantly with the scraper, exhibiting a sharp increase in the inclination angle to 28°, whereas the lower layer maintained a mixed flow–sliding motion (Fig. 11(c4)). Owing to the localized velocity differences, n decreased compared with the medium-speed stage, accompanied by a weakening of the overall force chain (Fig. 11(d_4)). The reduced N facilitated particle deposition into the powder bed, enabling stable spreading and uniform packing. However, at even higher spreading speeds, excessive inertial effects deprived particles of sufficient time for vertical deposition, ultimately compromising the uniformity of the powder bed.

Figs. 9 (a_3–d_3) and 12 show the motion characteristics and stress status of the GA0–53 powder particles at different spreading speeds. As the spreading speed increased from 35 to 155 mm/s, the variation in the particle velocities led to a reduction in n, causing N to decrease. This facilitated particle flow into the gaps and deposition into the powder bed, thereby improving the packing density. At high speeds (215 mm/s), the powder pile ahead of the scraper transitioned into a rigid bulk state owing to the inertial effect, which drove it forward as a whole along the scraper's advancing direction. The relative flow and sliding between the internal particles decreased significantly (as shown in Fig. 9(d_3)), whereas n increased. Concurrently, F between particles increased, resulting in a notable increase in N to 2.6×10^{-7} N (Figs. 8(d) and 12(d_4)). Consequently, this impeded the downward filling tendency of the particles, resulting in a packing density that dropped below 15 %. Owing to the higher proportion of irregular particles in GA0–53 powder, its n remains elevated, and N under all spreading parameters was more than twice that of the other powders (Fig. 8(d)), demonstrating a stronger contact effect. During spreading, the weak flow of particles in the front powder pile made filling the gaps difficult, resulting in a consistently low packing density across all parameters (see Section 3.1). Moreover,

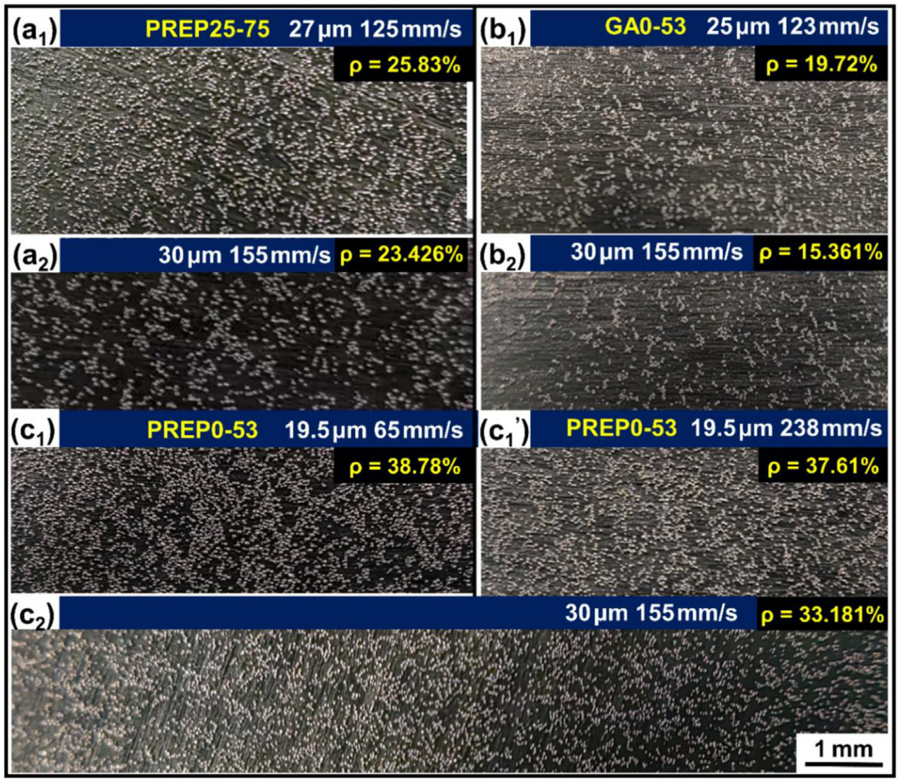

Fig. 13. Comparison of the powder beds under (a_1) (b_1) (c_1) (c_1') optimized spreading parameters and (a_2) (b_2) (c_2) the equipment's default parameters for (a_1) (a_2) PREP25–75, (b_1) (b_2) GA0–53, and (c_1) (c_1') (c_2) PREP0–53.

poor flowability tended to form localized uplifts near the rear of the powder pile adjacent to the scraper, forming inclination angles of up to 39° (Fig. 12(c4)).

In summary, for these three powders with different characteristics, excellent powder-spreading quality was achieved when the spreading parameters fell within the range where the inertial effect was weak and the contact force was minimized (Fig. 13). Specifically, powders with a wide particle-size distribution (PREP25–75) exhibited more significant inertial effects owing to the presence of large particles during spreading, whereas powders with low sphericity and irregular morphology (GA0–53) showed stronger contact effects owing to enhanced interparticle friction and mechanical interlocking. In contrast, powders with a narrow particle size distribution and high sphericity (PREP0–53) exhibited relatively low inertial and contact effects, enabling balanced behavior and optimal spreading performance at both low and medium-to-high spreading speeds.

5. Conclusions

This study established an adaptive powder-spreading strategy for LPBF by integrating DEM simulations and ML for three types of TC4 powders to rapidly optimize the layer thickness and spreading speed based on powder characteristics. This strategy is expected to be extendable to powders with other characteristics and to different alloy systems. The main conclusions are as follows:

(1) A DEM–ML integrated framework enables rapid adaptive optimization of the LPBF spreading parameters for diverse powders. By combining DEM simulations (calibrated with in-situ monitoring of particle dynamics) and an SVM model trained on the simulation data, this study established a method to intelligently optimize the powder layer thickness and spreading speed based on specific powder characteristics (particle size distribution and morphology). This approach achieves a 93 % prediction accuracy and significantly reduces the need for costly trial-and-error experiments while improving the surface roughness (*Ra*) by 26.5 %–37.9 % for PREP and GA TC4 powders compared with default parameters.

(2) The optimal spreading parameters are powder-specific and depend on inherent characteristics. The PREP0–53 powder (smaller, spherical particles) achieved excellent fusion quality across a wider range of spreading speeds (both low and medium-high), benefiting from better flowability. PREP25–75 powder (larger particles) performed best at medium speeds, as high speeds exacerbated the inertial effects and low speeds offered fewer advantages. The GA0–53 powder (irregular morphology) required medium spreading speeds to balance the flowability limitations and inertial effects, achieving the best (though still lower) packing density and fusion quality under these conditions. Crucially, the highest packing density does not always correlate with the best fusion surface quality, underscoring the need for an integrated optimization approach.

(3) Powder-spreading quality is governed by the inertial effects and contact effects. DEM simulations and in-situ monitoring revealed that optimal packing density and uniformity occurred when the spreading parameters minimized the interparticle contact forces while avoiding excessive inertial effects. Weak inertial effects (lower speeds) enable particle flow and rearrangement for improved packing, whereas minimized contact forces (achieved at specific speeds depending on the powder type) facilitate particle filling under gravity. Strong inertial effects (high speeds) cause rigid powder pile motion and poor filling, whereas high contact forces (especially in irregular powders such as GA) hinder vertical flow and gap filling.

Data availability

The data that support this study are available from the corresponding author upon reasonable request.

Declaration of competing interest

The authors declare that they have no known competing financial interests or personal relationships that could have appeared to influence the work reported in this paper.

CRediT authorship contribution statement

Yiqi Peng: Writing – original draft, Investigation, Formal analysis, Data curation. **Yaru Fan:** Writing – review & editing, Visualization, Investigation, Data curation. **Yufan Zhao:** Writing – review & editing, Supervision, Project administration, Methodology, Funding acquisition. **Hao Wang:** Methodology, Conceptualization. **Sirui Zhang:** Writing – review & editing, Visualization, Data curation. **Kenta Aoyagi:** Writing – review & editing, Conceptualization. **Seunkyun Yim:** Data curation, Conceptualization. **Akihiko Chiba:** Writing – review & editing, Conceptualization. **Xin Lin:** Supervision, Project administration, Funding acquisition.

Acknowledgements

This work was supported by National Natural Science Foundation of China (Grant No. 52305422), National Key R&D Program of China (Grant Nos. 2022YFB4600800 and 2023YFB3712000), and the Guangdong Basic and Applied Basic Research Foundation (Grant No. 2022A1515110242).

Supplementary materials

Supplementary material associated with this article can be found, in the online version, at doi:10.1016/j.amf.2025.200274.

References

[1] Chandra S, Wang C, Tor SB, et al. Powder-size driven facile microstructure control in powder-fusion metal additive manufacturing processes. Nat Commun 2024;15(1):3094. doi:10.1038/s41467-024-47257-w.
[2] Sutton AT, Sehhat MH, Leu MC, et al. Modeling powder spreadability in powder-based processes using the discrete element method. Addit Manuf 2024;92:104345. doi:10.1016/j.addma.2024.104345.
[3] Chen H, Cheng T, Li Z, et al. Is high-speed powder spreading really unfavourable for the part quality of laser powder bed fusion additive manufacturing? Acta Mater 2022;231:117901. doi:10.1016/j.actamat.2022.117901.
[4] Engeli R, Etter T, Hövel S, et al. Processability of different IN738LC powder batches by selective laser melting. J Mater Process Technol 2016;229:484–91. doi:10.1016/j.jmatprotec.2015.09.046.
[5] Sun P, Fang ZZ, Zhang Y, et al. Review of the methods for production of spherical Ti and Ti alloy powder. JOM 2017;69(10):1853–60. doi:10.1007/s11837-017-2513-5.
[6] Hu Z, Chen H, Yang Z, et al. Critical role of electrostatic forces in powder spreading in micro laser powder bed fusion. Addit Manuf 2025;109:104848. doi:10.1016/j.addma.2025.104848.
[7] Hyer HC, Petrie CM. Effect of powder layer thickness on the microstructural development of additively manufactured SS316. J Manuf Process 2022;76:666–74. doi:10.1016/j.jmapro.2022.02.047.
[8] Ghadi S, Chen X, Tomasello NS, et al. Modulated laser thermal interrogation (MLTI): a novel in situ metal powder evaluation technique for laser powder bed fusion. Addit Manuf 2025;102:104728. doi:10.1016/j.addma.2025.104728.
[9] Kleba-Ehrhardt R, Jastram B, Heinze C, et al. Effect of relative humidity on powder flowability and powder bed formation in additive manufacturing. Addit Manuf 2025;109:104862. doi:10.1016/j.addma.2025.104862.
[10] Asherloo M, Ramadurai MS, Heim M, et al. Advancing laser powder bed fusion with non-spherical powder: powder-process-structure-property relationships through experimental and analytical studies of fatigue performance. Addit Manuf 2024;95:104534. doi:10.1016/j.addma.2024.104534.
[11] Talebi FA, Haydari Z, Salehi H, et al. Spreadability of powders for additive manufacturing: a critical review of metrics and characterisation methods. Particuology 2024;93:211–34. doi:10.1016/j.partic.2024.06.013.
[12] Schiochet Nasato D, Pöschel T. Influence of particle shape in additive manufacturing: discrete element simulations of polyamide 11 and polyamide 12. Addit Manuf 2020;36:101421. doi:10.1016/j.addma.2020.101421.
[13] Sanders B, Cant E, Jenkins M. *Re*-use of polyamide-12 in powder bed fusion and its effect on process-relevant powder characteristics and final part properties. Addit Manuf 2024;80:103961. doi:10.1016/j.addma.2024.103961.
[14] Ren P, Ouyang Y, Mu J, et al. Metal powder atomization preparation, modification, and reuse for additive manufacturing: a review. Prog Mater Sci 2025;152:101449. doi:10.1016/j.pmatsci.2025.101449.
[15] Yim S, Bian H, Aoyagi K, et al. Spreading behavior of Ti-48Al-2Cr-2Nb powders in powder bed fusion additive manufacturing process: experimental and discrete element method study. Addit Manuf 2022;49:102489. doi:10.1016/j.addma.2021.102489.
[16] Meier C, Weissbach R, Weinberg J, et al. Critical influences of particle size and adhesion on the powder layer uniformity in metal additive manufacturing. J Mater Process Technol 2019;266:484–501. doi:10.1016/j.jmatprotec.2018.10.037.
[17] Lampitella V, Trofa M, Astarita A, et al. Discrete element method analysis of the spreading mechanism and its influence on powder bed characteristics in additive manufacturing. Micromachines (Basel) 2021;12(4):392. doi:10.3390/mi12040392.
[18] Le T-P, Wang X, Davidson KP, et al. Experimental analysis of powder layer quality as a function of feedstock and recoating strategies. Addit Manuf 2021;39:101890. doi:10.1016/j.addma.2021.101890.
[19] Chen H, Chen Y, Liu Y, et al. Packing quality of powder layer during counter-rolling-type powder spreading process in additive manufacturing. Int J Mach Tools Manuf 2020;153:103553. doi:10.1016/j.ijmachtools.2020.103553.
[20] Chen H, Wei Q, Zhang Y, et al. Powder-spreading mechanisms in powder-bed-based additive manufacturing: experiments and computational modeling. Acta Mater 2019;179:158–71. doi:10.1016/j.actamat.2019.08.030.
[21] Brika SE, Letenneur M, Dion CA, et al. Influence of particle morphology and size distribution on the powder flowability and laser powder bed fusion manufacturability of Ti-6Al-4V alloy. Addit Manuf 2020;31:100929. doi:10.1016/j.addma.2019.100929.
[22] Di Maio F, Di Renzo A. Modelling particle contacts in distinct element simulations: linear and non-linear approach. Chem Eng Res Des 2005;83(11):1287–97. doi:10.1205/cherd.05089.
[23] Mao K, Wang MY, Xu Z, et al. DEM simulation of particle damping. Powder Technol 2004;142(2–3):154–65. doi:10.1016/j.powtec.2004.04.031.
[24] Zhao Y, Koizumi Y, Aoyagi K, et al. Thermal properties of powder beds in energy absorption and heat transfer during additive manufacturing with electron beam. Powder Technol 2021;381:44–54. doi:10.1016/j.powtec.2020.11.082.
[25] Shaheen M, Thornton A, Luding S, et al. Discrete particle simulation of the spreading process in additive manufacturing https://research.utwente.nl/en/publications/discrete-particle-simulation-of-the-spreading-process-in-additive/.
[26] Spurek MA, Sillani F, Haferkamp L, et al. Effect of powder properties, process parameters, and recoating speed on powder layer properties measured by in-situ laser profilometry and part properties in laser powder bed fusion. Addit Manuf 2024;95:104512. doi:10.1016/j.addma.2024.104512.
[27] Emminghaus N, Hoff C, Hermsdorf J, et al. Residual oxygen content and powder recycling: effects on surface roughness and porosity of additively manufactured Ti-6Al-4V. Addit Manuf 2021;46:102093. doi:10.1016/j.addma.2021.102093.
[28] Zhao Y, Bian H, Wang H, et al. Non-equilibrium solidification behavior associated with powder characteristics during electron beam additive manufacturing. Mater Des 2022;221:110915. doi:10.1016/j.matdes.2022.110915.
[29] Mussatto A, Groarke R, O'Neill A, et al. Influences of powder morphology and spreading parameters on the powder bed topography uniformity in powder bed fusion metal additive manufacturing. Addit Manuf 2021;38:101807. doi:10.1016/j.addma.2020.101807.
[30] Yim S, Bian H, Aoyagi K, et al. Effect of powder morphology on flowability and spreading behavior in powder bed fusion additive manufacturing process: a particle-scale modeling study. Addit Manuf 2023;72:103612. doi:10.1016/j.addma.2023.103612.
[31] Shi S, Zhao Y, Lin X, et al. Significance of α-Al cellular matrix in tensile behavior and work-hardening of additive manufactured AlSi10Mg alloy. Virt Phys Prototyp 2025;20(1):e2449189. doi:10.1080/17452759.2024.2449189.
[32] Wang J, Zhu R, Liu Y, et al. Understanding melt pool characteristics in laser powder bed fusion: an overview of single- and multi-track melt pools for process optimization. Adv Powder Mater 2023;2(4):100137. doi:10.1016/j.apmate.2023.100137.
[33] Takaku K, Suzuki S, Ikeshoji T-T, et al. Assessing powder processability and melting behavior in powder-bed fusion additive manufacturing. Mater Des 2024;240:112877. doi:10.1016/j.matdes.2024.112877.
[34] Zhao Y, Aoyagi K, Cui Y, et al. Multiscale heat transfer affected by powder characteristics during electron beam powder-bed fusion. Powder Technol 2023;421:118438. doi:10.1016/j.powtec.2023.118438.
[35] Nan W, Pasha M, Ghadiri M. Numerical simulation of particle flow and segregation during roller spreading process in additive manufacturing. Powder Technol 2020;364:811–21. doi:10.1016/j.powtec.2019.12.023.
[36] Yim S, Wang H, Aoyagi K, et al. Comparative evaluation of powder spreading strategies to enhance powder bed quality in powder bed fusion additive manufacturing: a DEM simulation study. Powder Technol 2025;453:120614. doi:10.1016/j.powtec.2025.120614.
[37] Sun Y, Aindow M, Hebert RJ. Comparison of virgin Ti-6Al-4V powders for additive manufacturing. Addit Manuf 2018;21:544–55. doi:10.1016/j.addma.2018.02.011.
[38] Yim S, Wang H, Aoyagi K, et al. Role of gravity magnitude on flowability and powder spreading in the powder bed fusion additive manufacturing process: towards additive manufacturing in space. Addit Manuf 2024;94:104441. doi:10.1016/j.addma.2024.104441.